

## On the Specification of Upward-Propagating Tides for ICON Science Investigations

Jeffrey M. Forbes · Xiaoli Zhang ·  
Maura E. Hagan · Scott L. England ·  
Guiping Liu · Federico Gasperini

Received: date / Accepted: date

**Abstract** The National Center for Atmospheric Research (NCAR) Thermosphere Ionosphere Electrodynamics General Circulation Model (TIEGCM) will provide a physics-based context for the interpretation of ICON measurements. To optimize the realism of the model simulations, ICON wind and temperature measurements near the  $\sim 97$  km lower boundary of the TIEGCM will be used to specify the upward-propagating tidal spectrum at this altitude. This will be done by fitting a set of basis functions called Hough Mode Extensions (HMEs) to 27-day mean tidal winds and temperatures between 90 and 105 km altitude and between  $12^\circ\text{S}$  and  $42^\circ\text{N}$  latitude on a day-by-day basis. The current paper assesses the veracity of the HME fitting methodology given the restricted latitude sampling and the UT-longitude sampling afforded by the MIGHTI instrument viewing from the ICON satellite, which will be in a circular  $27^\circ$  inclination orbit. These issues are investigated using the output from a reanalysis-driven global circulation model, which contains realistic variability of the important tidal components, as a mock data set. ICON sampling of the model reveals that the 27-day mean diurnal and semidiurnal tidal components replicate well the 27-day mean tidal components obtained from full synoptic sampling of the model, but the terdiurnal tidal components are not faithfully reproduced. It is also demonstrated that reconstructed tidal

---

Jeffrey M. Forbes, Xiaoli Zhang and Federico Gasperini  
Department of Aerospace Engineering Sciences  
University of Colorado, Boulder, CO 80305  
Tel.: +1-303-735-0551  
Fax: +1-303-492-7881  
E-mail: forbes@colorado.edu

Maura E. Hagan  
Department of Physics  
Utah State University, Logan, UT 84332

Scott L. England and Guiping Liu  
Space Sciences Laboratory  
University of California, Berkeley, CA 94720

components based on HME fitting to the model tides between 12°S and 42°N latitude provide good approximations to the major tidal components expected to be encountered during the ICON mission. This is because the constraints provided by fitting both winds and temperatures over the 90-105 km height range are adequate to offset the restricted sampling in latitude. The boundary conditions provided by the methodology described herein will greatly enhance the ability of the TIEGCM to provide a physical framework for interpreting atmosphere-ionosphere coupling in ICON observations due to atmospheric tides.

**Keywords** ICON · Tides · TIEGCM · Boundary Conditions

## 1 Introduction

Within the ICON Mission, the Thermosphere Ionosphere Electrodynamics General Circulation Model (TIEGCM) [Richmond et al., 1992; Qian et al., 2014; see also Maute et al., 2016, this issue] will play a key role in providing physics-based relationships between neutral winds, neutral temperatures, electron densities, plasma drifts, neutral and ion compositions and underlying chemical reactions, that are relevant to interpretation of ICON measurements. The TIEGCM will be forced by the three main energy sources relevant to the ionosphere-thermosphere (IT) system: solar photon radiation, energy and momentum inputs at high latitudes from the magnetosphere, and energy and momentum input in the form of upward-propagating waves at the  $\sim 97$  km altitude lower boundary (LB) of the TIEGCM. The first two energy inputs are described in papers by Maute et al. [2016] and Crowley et al. [2016], respectively, in this special issue. The present paper deals with the specification of waves at the LB of the TIEGCM.

The waves of relevance to the IT are gravity waves (GW), tides and planetary waves (PW). Recent theory and modeling indicate that upward-propagating tides, GW and PW are potentially important to both the mean structure and variability of the IT [e.g., Forbes et al., 1993; Jones et al., 2014; Yiğit and Medvedev, 2010, 2015; Vadas and Liu, 2009, 2013; Miyoshi et al., 2014; Nguyen and Palo, 2014; Yue and Wang, 2014]. However, the GW spectrum near 97 km on a global scale is unknown, and the ICON measurements are not well suited to capture GW; consequently, GW are not part of ICON core science and no GW specification at the TIEGCM LB will be attempted. Relatedly, the TIEGCM will not resolve the seasonal-latitudinal structure of the mesopause region produced by GW momentum deposition. With regard to PW, the 12°S to 42°N latitude range of ICON wind and temperature measurements (see below), and the strong departure of PW structures from those of classical wave theory due to the effects of mean winds, precludes any credible specification of PWs at the LB of the TIEGCM. [Note: If TIMED/SABER temperature measurements are still available during the ICON mission, LB specification of PW could be possible.] In contrast, tidal structures near 97 km are known to be reasonably well expressed [Oberheide et al., 2011] in terms

of latitudinal expansion functions from tidal theory [Forbes and Hagan, 1982], which opens the possibility that ICON data can be used to specify tides at the LB of the TIEGCM, and thus optimize the realism of model simulations for various ICON science investigations. The primary focus of the present paper is to assess the veracity of applying this methodology given the spatial-temporal sampling afforded by ICON observations.

The following Section reviews some basic tidal nomenclature, and Section 3 describes the so-called ‘‘Hough Mode Extension (HME)’’ methodology used to fit and decompose ICON tidal structures such that TIEGCM LB conditions can be specified. Section 4 assesses how the asymptotic UT-longitude sampling of ICON affects the determination of tidal components from ICON measurements, and Section 5 quantifies how the ICON latitudinal coverage impacts the HME fitting process. A summary and conclusions are provided in Section 6.

## 2 Tidal Nomenclature

Atmospheric tides are oscillations excited by the release of heat due to absorption of solar radiation in an atmosphere that is rotating with respect to the Sun. Absorption of IR radiation by tropospheric  $H_2O$  and UV radiation by stratospheric  $O_3$  as well as latent heat release in deep tropical clouds excite a spectrum of thermal tides in the lower atmosphere. This heating distribution and the oscillations that are produced by it are therefore expressible mathematically in terms of periodic functions in time and longitude:

$$\sum_{s=-k}^{s=+k} \sum_{n=1}^N A_{n,s}(z, \theta) \cos(n\Omega t + s\lambda - \phi_{n,s}(z, \theta)) \quad (1)$$

where  $n = 1, 2, 3$  refers to diurnal, semidiurnal and terdiurnal (periods of 24h, 12h, 8h, respectively);  $s$  is the zonal wavenumber;  $t$  is universal time;  $\lambda$  is longitude;  $\phi$  is the phase;  $z$  is altitude and  $\theta$  is latitude. The spectrum of waves is filtered by mean winds and dissipation as they propagate upward and grow exponentially with altitude up to  $\sim 100$ -150 km, where molecular dissipation curtails further exponential growth. Only the waves with longest vertical wavelengths ( $> 50$  km) penetrate to upper levels in the thermosphere, but composition effects that are induced in the lower thermosphere are effectively transmitted upward by molecular diffusion.

The part of the above expression that is in parentheses on the right-hand side of (1) implies the following zonal (east-west) phase speeds of the individual terms in the expansion:  $C_{ph} = -\frac{n\Omega}{s}$  where  $s < 0$  ( $s > 0$ ) implies eastward (westward) propagating waves. Waves with  $s \neq n$  are called non-migrating tides; they capture the longitude dependence of the tidal response. The migrating (sun-synchronous) tides ( $s = n$ ) are longitude-independent. We utilize the notation DWs or DEs to denote a westward or eastward-propagating diurnal

tide, respectively, with zonal wavenumber =  $s$ . For semidiurnal and terdiurnal oscillations ‘S’ and ‘T’ respectively replaces ‘D’. The zonally-symmetric oscillations are denoted D0, S0, T0.

### 3 Hough Mode Extensions (HMEs) and Characterization of Tidal Structures

The concept of HMEs was developed by Lindzen et al. [1977] and Forbes and Hagan [1982] in order to deal with the changes in shape of Hough modes as they encounter dissipation in an atmospheric regime above that of wave forcing. A Hough mode extension represents the global solution (pole-to-pole, 0-to-400-km altitude) to the linearized dynamical equations of the atmosphere for an oscillation of given frequency and zonal wavenumber, taking into account dissipative effects (i.e., radiative cooling, eddy and molecular diffusion of heat and momentum) above the forcing region [e.g., Forbes, 1982; Hagan, 1996; Hagan et al., 1995, 1999; Hagan and Forbes, 2002, 2003], while setting background winds and meridional gradients of temperature, density and pressure equal to zero. The HMEs are forced with a conveniently normalized heat source in the troposphere, and with latitude shape given by the corresponding classical Hough mode. For a given zonal wavenumber and wave period, a HME can be thought of as a latitude versus height table of amplitudes and phases for the velocity, temperature and density perturbation fields  $(u, v, w, T, \rho)$  of the oscillation. The  $(u, v, w, T, \rho)$  perturbation fields maintain internally self-consistent relative amplitude and phase relationships for any given HME. So, if the amplitude and phase of the perturbation wind field is known for a given HME at a single latitude and height, then all the fields  $(u, v, w, T, \rho)$  are known for all latitudes and all heights.

When HMEs are fit to data (in a least-squares sense) only a single complex normalizing coefficient (or equivalently, a single amplitude factor and phase shift) is sought for each HME. HMEs can be fit simultaneously to observed temperature, wind and density variations at any combination of latitudes and altitudes. Examples of the amplitude and phase structures of temperature and meridional wind for the first symmetric and first antisymmetric HMEs for DE3 are provided in Figure 1. The amplitudes and phases of HMEs are arbitrary. The higher-order modes have progressively greater numbers of nodes in latitude, and shorter vertical wavelengths. Since the importance of molecular dissipation varies inversely as the square of the vertical wavelength [Forbes and Garrett, 1979], higher-order modes are less capable of penetrating to higher altitudes than lower-order modes.

Although zonal mean winds are neglected in the computation of HMEs, this does not imply that the effects of mean winds are neglected in fitting or reconstructing tidal structures. To first order, the distortion of tidal structures due to mean winds can be viewed as mode coupling [Lindzen and Hong 1974]; that is, the excitation of higher-order modes that combine together in a linear sense to approximate the distortion. In the same sense, a few HMEs can be

fit to a tidal field in a way that the weighted superposition of these HMEs reproduces the observed distortion. The methodology assumes that all of the important mean-wind effects occur below the region in which the HME fitting occurs; that is, in association with the mesospheric jets; in other words, that the 80-100 km winds are too weak to produce any significant additional distortion of the tidal structures.

The methodology for fitting HMEs to observational data is fully described in Forbes et al. [1994]. These authors used HMEs for the migrating semidiurnal tide to simultaneously fit semidiurnal tidal winds and temperatures between 80 and 150 km, and by reconstruction arrived at a monthly climatological model of horizontal and vertical winds, temperatures and densities in this height region. Subsequently, Svoboda et al. [2005] and Oberheide et al. [2011] utilized HMEs to fit Upper Atmosphere Research Satellite (UARS) and Thermosphere Ionosphere Mesosphere Energetics and Dynamics (TIMED) satellite data, respectively, in the lower thermosphere to similarly arrive at internally-consistent global climatologies of tidal temperatures, winds and densities in the 80-120 km height region.

Svoboda et al. [2005] validated the method using output from the Kyushu University General Circulation Model as a mock data set. For instance, they verified that fitting tidal temperature fields alone led to calibrated HMEs that replicated the corresponding model tidal wind fields. The reader is referred to Forbes et al. [1994] and Svoboda et al. [2005] for further information and details on the HME technique, its applications and limitations; and to Oberheide [2011] for important validations of HME tidal fields at higher altitudes in the thermosphere.

The work of Oberheide et al. [2011] resulted in the Climatological Tidal Model of the Thermosphere (CTMT), and the CTMT is currently an option for the lower boundary tidal specification in the TIEGCM. However, the CTMT is based on fits to 60-day mean tidal fields averaged over 2002-2008. We tacitly assume that application of HME fitting to 27-day mean ICON data for this purpose will yield more realistic TIEGCM simulations of neutral winds, temperatures, plasma densities and drifts for contemporaneous ICON science investigations, as compared with use of CTMT. However, it must be demonstrated that the method is robust given the UT-longitude and latitude sampling provided by ICON. These issues are addressed in the following sections.

#### **4 Impacts of ICON UT-Longitude Sampling on the Extraction of Tides**

Before fitting HMEs to any given tidal component, that tidal component must first be retrieved from the data at hand. Extraction of solar tides from atmospheric data generally requires 24 hours of local time coverage, although semidiurnal and higher-order tidal harmonics can be reliably determined from observations covering a fraction of a day under the right conditions [Crary and

Forbes, 1985]. Since diurnal tides such as DW1, DE3 and DE2 will play an important role in ICON science, specification of diurnal tides at the TIEGCM LB is necessary and 24 hours of local time (LT) coverage is required.

The requirement of complete LT coverage applies at all the latitudes and longitudes where the relevant measurements from ICON are acquired, i.e., winds and temperatures from the MIGHTI instrument [Englert et al., 2016] between 12°S and 42°N latitude and 90-105 km altitude. However, ICON/MIGHTI's sampling is not *synoptic* within these domains; that is, at a given height and latitude, not all UTs are sampled simultaneously across all longitudes. In fact, for ICON's orbital configuration it takes 27 days to acquire measurements over 24 hours of local time across the full range of latitudes and longitudes. A few examples of latitude-longitude-LT sampling are provided in Figure 2. The question arises, then, how representative is this 27-day characterization of the actual fully-sampled atmosphere, and how well do the tidal components derived from it compare with those obtained from the fully-sampled result? This question is addressed immediately below by deriving tides from a realistically-variable global numerical simulation according to ICON sampling (e.g., Figure 2), and comparing these results with those obtained from the fully sampled simulation.

The model chosen for these numerical experiments is the NCAR (National Center for Atmospheric Research) TIME-GCM (Thermosphere Ionosphere Mesosphere Electrodynamics General Circulation Model) forced at its  $\sim 30$ -km lower boundary by global reanalysis data during 2009 from MERRA (Modern-Era Retrospective Analysis for Research and Applications as described in Häusler et al. [2014, 2015]). The TIME-GCM is the latest in the series of global time-dependent NCAR models developed to simulate the circulation, temperature, electrodynamics, and compositional structure of the upper atmosphere and ionosphere. The TIME-GCM is a global grid point model that calculates neutral gas heating, dynamics, photoionization, electrodynamics, and the compositional structure of the middle and upper atmosphere and ionosphere from first principles for a given solar irradiance spectrum. The TIME-GCM inherently accounts for atmospheric tides that are excited by the absorption of ultraviolet and extreme ultraviolet radiation in the middle and upper atmosphere. Upward-propagating waves excited in the troposphere are specified at the  $\sim 30$  km lower boundary of the TIME-GCM (see below). The upper boundary of the TIME-GCM for this solar minimum simulation is near 500 km. Subgrid-scale gravity waves are necessary for realistic simulations of the mesopause region and are parameterized with a modified Lindzen [1981]-type scheme that is extended to include molecular damping effects in the lower thermosphere. See Roble and Ridley [1994] and Roble [1995] for a more complete description.

As described in Häusler et al. [2014, 2015], the 2009 TIME-GCM simulation is forced by interpolated 3-hourly MERRA dynamical fields at the lower boundary of  $\sim 30$  km. This simulation uses a  $2.5^\circ \times 2.5^\circ$  grid resolution in latitude and longitude, four grid points per scale height in the vertical direction, and 60-second time step, although only hourly histories are archived.

This resolution is necessary in order to resolve the waves of interest in this study. F10.7 values and cross-cap potentials based on Kp indices are used to nominally represent solar radiative and high-latitude forcing during this solar minimum and geomagnetically quiescent year-long period.

MERRA is a NASA satellite-era reanalysis that uses a major new version of the Goddard Earth Observing System Data Assimilation System Version 5 (GEOS-5) [Rienecker et al., 2011]. It has a horizontal resolution of  $1.25^\circ$ , temporal resolution of 3h and 42 vertical levels from 1000hPa to 0.1hPa ( $\sim 64$  km). It is a physics-based weather prediction model constrained by global data. It was chosen for this investigation due to its comprehensive nature, especially in terms of the hydrological cycle which is relevant to tidal and ultra-fast Kelvin wave (UFKW) forcing. There is a large number of papers that have used MERRA to study regional and global climate, various types of wave coupling, precipitation, stratospheric water vapor, global energy and water budgets, etc., and some sort of validation is part of all of these studies. A study by Lindsay et al. [2014] evaluates 7 different reanalysis products (including several versions of NCEP, ECMWF, and MERRA) and finds MERRA to out-perform the others. A particular strength of MERRA is the availability of 3-hourly data, whereas other publicly available reanalysis/assimilation products are 6-hourly.

Figure 3 provides evidence that the MERRA-forced TIME-GCM reflects realistic tidal variability. In this figure, daily DE3 tidal temperatures from TIMED/SABER measurements at 100 km are compared with those from the model. The degree of day-to-day variability is similar, and the observed maximum activity period for DE3 between days 180-240 is also well approximated by the model. The observed variability is likely due to some combination of source variability (i.e., latent heating associated with tropical convection), variability of the DE3 propagation environment, and planetary wave-tide interactions. The day-to-day variability of DE3 is approximated by taking differences in measurements between ascending and descending parts of the orbit, assuming these differences are close enough to 12 hours to produce minimal aliasing. Some modest reduction in DE3 amplitudes, and possible aliasing due to SE2, are expected due to the 9-hour difference between ascending and descending parts of the TIMED orbit [Oberheide et al., 2003a,b]. However, this does not impact our qualitative assessment concerning the level of tidal variability in the model simulations. Based on prior modeling and theory [Forbes et al., 2001, 2003a,b, 2006, Hagan and Forbes, 2002], DE3 is arguably the only tidal component for which this can be done with reasonable confidence, as DE3 is the only physically plausible diurnal tide that appears as wave-4 in longitude as viewed from space in a quasi-constant local time frame. We furthermore note that ICON/MIGHTI sampling will not be well suited for production of such a daily DE3 proxy.

Figures 4-6 compare some typical tidal temperature components derived from fully-sampled and ICON-sampled model data for the first 3 months of 2009. In each of these plots, the left panel illustrates the daily tidal amplitudes, the middle panel shows the fully-sampled (true) results obtained from 27-day windows slipped forward one day at a time, and the right panel illustrates

the corresponding ICON-sampled results. Figure 4 demonstrates that the two largest diurnal tides, DW1 and DE3, are well approximated by ICON sampling. Similar fidelity is obtained for DE2 and DW2 (not shown). Results in Figure 5 for the largest semidiurnal tides, SW2 and SE2, also show good consistency between fully-sampled and ICON sampled results, and similar consistency exists for (not shown) SW4 (max amplitude  $\sim 5K$ ) and SW5 (max amplitude  $\sim 3K$ ). Latitude vs. DOY structures for DE1 and SE1 are not as well approximated, but these tidal components have amplitudes less than about 2K. Figure 6 shows some typical comparisons for terdiurnal tidal components, here TW3 and TE1. None of the terdiurnal components extracted from the fully-sampled model are reasonably approximated by the ICON-sampled results.

## 5 Impacts of ICON Latitude Sampling on HME-Fitting of Tidal Structures

Focusing on the major diurnal and semidiurnal components revealed in the MERRA-forced TIME-GCM simulation, we now examine to what degree tidal components can be reasonably be expressed in terms of HMEs where the fitting of the tidal components is restricted to the  $12^\circ S$  to  $42^\circ N$  latitude range. The following results were obtained by simultaneously fitting 27-day-mean temperature and zonal and meridional wind tidal components between 90 and 105 km and  $12^\circ S$  to  $42^\circ N$  latitude. Simultaneously fitting multiple parameters over a range of heights provides important constraints that compensate for the limited latitudinal coverage. As checks on our understanding, fits were performed using fewer tidal parameters, as well as latitude ranges  $84^\circ S$  to  $84^\circ N$  and  $42^\circ S$  to  $42^\circ N$ , but these results are not shown here. For each tidal component, the number of HMEs fit is determined by the vertical wavelength; the HME series for a given tidal component is truncated such that HMEs with vertical wavelengths less than 25 km are excluded from the fit, since these waves are very inefficient in propagating above 100 km due to dissipation. In general 4 HMEs are fit to each tidal component; the exceptions are DW1 and DW2, where only the first symmetric HME is fit.

Figure 7 illustrates comparisons between TIMEGCM tidal components DE3 and DW1 (left panels), and those obtained by reconstruction using HME fits (right panels) to these same tidal components as described above. Also shown are correlation coefficients ( $R$ ) between the left and right panels. The quantity  $R^2$  provides a measure of the variance captured by the HME reconstruction. Both DE3 and DW1 are replicated very well ( $R = 0.95$  and  $R = 0.93$ , respectively), despite the restricted latitude range used in fitting the HMEs. Similar results are obtained for DE2 ( $R = 0.95$ ) in Figure 8, and for DW2 ( $R = 0.95$ , not shown).

The fit shown in Figure 8 for D0 is not as good ( $R = 0.69$ ); however, fitting over  $84^\circ S$  to  $84^\circ N$  only increases the correlation coefficient to 0.74. This means that it is not the restricted latitude range that mainly accounts for the difference, but something more fundamental to the HME methodology

itself. We note two characteristics of D0 that distinguish it from the other tidal components shown in Figures 7 and 8: (a) the amplitudes are generally less than 2.0K; and (b) the amplitude distributions are more structured. Inability of the HME method to fully deal with both of these features lies in the fact that we have limited the fits to the first two antisymmetric and symmetric HMEs with period = 1.0 days and  $s = 0$ . In principle adding higher-order HMEs to the fit would capture these details, but they are not included for the following reasons. First, these higher-order HMEs have vertical wavelengths less than about 10 km, are highly susceptible to dissipation, and would be so damped at higher altitudes to be of no practical significance. For the same reason, the eddy diffusivity assumed in the GSWM below 100 km is poorly known, and likely to lead to poor approximations to the horizontal shapes of these higher-order HMEs due to dissipative broadening [Forbes and Hagan, 1982].

Similar comparisons for the semidiurnal tide are provided in Figures 9 and 10. The comparisons for SE2 and SW2 in Figure 9 show very good agreement ( $R = .89$  and  $R = .88$ , respectively). SW1 ( $R = 0.75$ ) and especially S0 ( $R = 0.38$ ) shown in Figure 10 reveal less fidelity, and only moderate improvement when full latitude coverage is employed ( $R = 0.84$  and  $R = 0.45$ , respectively). Other results (not shown) include SE1 ( $R = 0.68$ ), SW3 ( $R = 0.64$ ), SW4 ( $R = 0.52$ ), with similar moderate improvement when fitting to the model output occurs over a wide latitude range.

An alternative perspective on the quality of HME fitting and reconstruction is provided in Figure 11, where a few representative results are shown. The left columns provide the total residuals from the zonal mean in a latitude vs. longitude depiction at 0000 UT, and thus all of the tidal components present in the MERRA-forced TIMEGCM for January, April July and October (top to bottom). The middle column shows the HME reconstruction based on the all fits discussed earlier in this section. The right column provides scatter plots and correlation coefficients based on comparisons between the data in the first two columns. The correlations range between about  $R = 0.70$  and  $0.84$ , indicating that the HME reconstructions capture about 50-70% of the total tidal variance in the TIMEGCM. Results based on fitting between  $84^{\circ}\text{S}$   $84^{\circ}\text{N}$  only increases this range of variances to about 55-75%, verifying again that the limited latitudinal sampling afforded by ICON is not playing a major role in degrading the HME fitting process.

The results obtained above for temperatures were also obtained for zonal and meridional winds, with similar results and conclusions.

## 6 Summary and Conclusions

A methodology has been developed and validated whereby ICON wind and temperature measurement between 90 and 105 km altitude and  $12^{\circ}\text{S}$  and  $42^{\circ}\text{N}$  latitude can be used to globally specify the most important components of the tidal spectrum entering the IT system from below. The method will be used

to specify diurnal and semidiurnal tides at the  $\sim 97$  km lower boundary of the TIEGCM on a day-by-day basis, thus providing a physics-based framework for interpreting atmosphere-ionosphere coupling by tides within the ICON mission. In this paper it is determined that ICON sampling of the atmosphere will yield realistic specifications of diurnal and semidiurnal tides (but not terdiurnal tides) between  $12^\circ\text{S}$  and  $42^\circ\text{N}$  latitude, and that sampling this range of latitudes within the fitting scheme adequately meets the need for *global* specifications of the tidal components at the lower boundary of the TIEGCM.

**Acknowledgements** This work was supported in part by NASA through the University of California at Berkeley under Award 00008209 to the University of Colorado. M.E. Hagan's efforts were supported in part by the National Center for Atmospheric Research and by the NASA U.S. Participating Investigator Program through Grant NNX12AD26G to University of Colorado and Subaward 75900816 to Utah State University.

## References

1. Crary, D., and J.M. Forbes (1983), On the Extraction of Tidal Information from Observations Covering a Fraction of a Day, *Geophys. Res. Lett.* *10*, 580-582.
2. Crowley, G. (2016), Assimilative Mapping of Ionospheric Electrodynamics (AMIE) for the Ionospheric Connections (ICON) Explorer, *Space Sci. Rev.*, *this issue*.
3. Englert, C.R., Harlander, J.M., Brown, C.M., Marr, K.D., Miller, I.J., Stump, J.E., Hancock, J., Peterson, J., Kumler, J., Morrow, W.H., Mooney, T.A., Ellis, S., Mende, S.B., Harris, S.E., Stevens, M.H., Makela, J.J., Harding, B.J., and T.J. Immel (2016), Michelson Interferometer for Global High-resolution Thermospheric Imaging (MIGHTI): Instrument Design and Calibration, *Space Sci. Rev.*, *this issue*.
4. Forbes, J.M. and H.B. Garrett (1979), Theoretical Studies of Atmospheric Tides, *Rev. Geophys. Space Phys.* *17*, 1951-1981.
5. Forbes, J.M. (1982), Atmospheric Tides. I. Model Description and Results for the Solar Diurnal Component, *J. Geophys. Res.* *87*, 5222-5240.
6. Forbes, J. M., and M. E. Hagan (1982), Thermospheric extensions of the classical expansion functions for semidiurnal tides, *J. Geophys. Res.*, *87*, 5253-5259.
7. Forbes, J. M., R. G. Roble, and C. G. Fesen (1993), Acceleration, heating, and compositional mixing of the thermosphere due to upward propagating tides, *J. Geophys. Res.*, *98(A1)*, 3113-3121, doi:10.1029/92JA00442.
8. Forbes, J.M., Manson, A.H., Vincent, R.A., Fraser, G.J., Vial, F., Wand, R., Avery, S.K., Clark, R.R., Johnson, R., Roper, R., Schminder, R., Tsuda, T., and E.S. Kazimirovsky (1994), Semidiurnal Tide in the 80-150 km Region: An Assimilative Data Analysis, *J. Atmos. Terr. Phys.*, *56*, 1237-1250.
9. Forbes, J. M., X. Zhang, and M. E. Hagan (2001), Simulations of diurnal tides due to tropospheric heating from the NCEP/NCAR Reanalysis Project, *Geophys. Res. Lett.*, *28*, 3851-3854.
10. Forbes, J. M., X. Zhang, W. Ward, and E. Talaat (2003a), Nonmigrating diurnal tides in the thermosphere, *J. Geophys. Res.*, *108*, 1033, doi:10.1029/2002JA009262.
11. Forbes, J. M., M. E. Hagan, S. Miyahara, Y. Miyoshi, and X. Zhang (2003b), Diurnal nonmigrating tides in the tropical lower thermosphere, *Earth Planets Space*, *55*, 419-426.
12. Forbes, J.M., J. Russell, S. Miyahara, X. Zhang, S. Palo, M. Mlynczak, C.J. Mertens, and M. E. Hagan (2006), Troposphere-thermosphere tidal coupling as measured by the SABER instrument on TIMED during July-September 2002, *J. Geophys. Res.*, *111*, A10S06, doi:10.1029/2005JA011492.
13. Hagan, M.E., J.M. Forbes, and F. Vial (1995), On modeling migrating solar tides, *Geophys. Res. Lett.*, *22*, 893-896.
14. Hagan, M.E. (1996), Comparative Effects of Migrating Solar Sources on Tides in the Mesosphere and Lower Thermosphere, *J. Geophys. Res.*, *101*, 21213-21222.

15. Hagan, M.E., Burrage, M.D., Forbes, J.M., Hackney, J., Randel, W.J., and X.Zhang (1999), GSWM-98: Results for migrating solar tides, *J. Geophys. Res.*, *104*, 6813-6827.
16. Hagan, M.E., and J.M. Forbes (2002), Migrating and nonmigrating diurnal tides in the middle and upper atmosphere excited by tropospheric latent heat release, *J. Geophys. Res.*, *107(D24)*, 4754, doi:10.1029/2001JD001236.
17. Hagan, M.E., and J.M. Forbes (2003), Migrating and nonmigrating semidiurnal tides in the upper atmosphere excited by tropospheric latent heat release, *J. Geophys. Res.*, *108(A2)*, 1062, doi:10.1029/2002JA009466.
18. Häusler, K., M.E. Hagan, A.J.G. Baumgaertner, A. Maute, G. Lu, E. Doornbos, S. Bruinsma, J.M. Forbes, and F. Gasperini (2014), Improved short-term variability in the thermosphere-ionosphere-mesosphere-electrodynamics general circulation model, *J. Geophys. Res.*, doi: 10.1002/2014JA020006.
19. Häusler, K., M.E. Hagan, J.M. Forbes, X. Zhang, E. Doornbos, S. Bruinsma, and G. Lu (2015), Intra-annual variability of tides in the thermosphere from model simulations and in situ satellite observations, *J. Geophys. Res. Space Physics*, *120*, 751765, doi:10.1002/2014JA020579.
20. Jones, M., Jr., J.M. Forbes, M. E. Hagan, and A. Maute (2014), Impacts of vertically propagating tides on the mean state of the ionosphere-thermosphere system, *J. Geophys. Res. Space Physics*, *119*, 21972213, doi:10.1002/2013JA019744.
21. Lindsay, R., M. Wensnahan, A. Schweiger, and J. Zhang (2014), Evaluation of Seven Different Atmospheric Reanalysis Products in the Arctic, *J. Climate*, *27*, 25882606. doi: <http://dx.doi.org/10.1175/JCLI-D-13-00014.1>.
22. Lindzen, R.S., S.-S. Hong, and J.M. Forbes (1977), Semidiurnal Hough mode extensions in the thermosphere and their application, *Memo. Rept. 3442*, 69 pp., Nav. Res. Lab., Washington, D. C.
23. Lindzen, R. S. (1981), Turbulence and stress owing to gravity wave and tidal breakdown, *J. Geophys. Res.*, *86*, 97079714, doi:10.1029/JC086iC10p09707.
24. Lindzen R.S., Hong S.-S. (1974), Effects of mean winds and meridional temperature gradients on solar and lunar semidiurnal tides in the atmosphere, *J. Atmos. Sci.*, *31*, 14211466.
25. Maute, A. (2016), Thermosphere-Ionosphere-Electrodynamics General Circulation Model for the Ionospheric Connection Explorer: TIEGCM-ICON, *Space Sci. Rev.*, *this issue*.
26. Miyoshi, Y., H. Fujiwara, H. Jin, and H. Shinagawa (2014), A global view of gravity waves in the thermosphere simulated by a general circulation model, *J. Geophys. Res. Space Physics*, *119*, doi:10.1002/2014JA019848.
27. Oberheide, J., M. E. Hagan, and R. G. Roble, Tidal signatures and aliasing in temperature data from slowly precessing satellites, *J. Geophys. Res.*, *108*, 1055, doi 10.1029/2002JA009585, 2003a.
28. Oberheide, J., M. E. Hagan, and R. G. Roble, Correction to *Tidal signatures and aliasing in temperature data from slowly precessing satellites*, *J. Geophys. Res.*, *108*, 1213, doi:10.1029/2003JA009967, 2003.
29. Oberheide, J., J.M. Forbes, X. Zhang, and S.L. Bruinsma (2011), Climatology of upward propagating diurnal and semidiurnal tides in the thermosphere, *J. Geophys. Res.*, *116*, A11306, doi:10.1029/2011JA016784.
30. Qian, L., A.G. Burns, B.A. Emery, B. Foster, G. Lu, A. Maute, A.D. Richmond, R.G. Roble, S.C. Solomon, and W. Wang, The NCAR TIE-GCM: A community model of the coupled thermosphere/ionosphere system, in *Modeling the Ionosphere-Thermosphere System*, AGU Geophysical Monograph Series, 2014.
31. Richmond, A.D., E.C. Ridley, and R.G. Roble, A thermosphere/ionosphere general circulation model with coupled electrodynamics, *Geophys. Res. Lett.*, *6*, 601-604, 1992.
32. Rienecker, M.M., Max J. Suarez, Ronald Gelaro, Ricardo Todling, Julio Bacmeister, Emily Liu, Michael G. Bosilovich, Siegfried D. Schubert, Lawrence Takacs, Gi-Kong Kim, Stephen Bloom, Junye Chen, Douglas Collins, Austin Conaty, Arlindo da Silva, Wei Gu, Joanna Joiner, Randal D. Koster, Robert Lucchesi, Andrea Molod, Tommy Owens, Steven Pawson, Philip Pegion, Christopher R. Redder, Rolf Reichle, Franklin R. Robertson, Albert G. Ruddick, Meta Sienkiewicz, and Jack Woollen (2011), MERRA: NASA's Modern-Era Retrospective Analysis for Research and Applications, *J. Climate*, *24*, 36243648. doi: <http://dx.doi.org/10.1175/JCLI-D-11-00015.1>

33. Roble, R.G. (1995), The NCAR Thermosphere-Ionosphere-Mesosphere- Electrodynamics General Circulation Model (TIME-GCM), Ionosphere Models, *STEP Handbook on Ionospheric Models*, ed. R. W. Schunk, Utah State University.
34. Roble, R.G. and E.C. Ridley (1994), A thermosphere-ionosphere-mesosphere-electrodynamics general circulation model (TIME-GCM): Equinox solar cycle minimum simulations (30500 km), *Geophys. Res. Lett.*, *21*, 417-420.
35. Svoboda, A.A., J.M. Forbes, and S. Miyahara (2005), A space-based climatology of temperatures and densities from diurnal MLT tidal winds, UARS wind measurements, *J. Atmos. Sol. Terr. Phys.*, *67(16)*, 15331543.
36. Vadas, S.L., and H. Liu (2009), Generation of large-scale gravity waves and neutral winds in the thermosphere from the dissipation of convectively generated gravity waves, *J. Geophys. Res.*, *114*, A10310, doi:10.1029/2009JA014108.
37. Vadas, S.L., and H. Liu (2013), Numerical modeling of the large-scale neutral and plasma responses to the body forces created by the dissipation of gravity waves from 6 h of deep convection in Brazil, *J. Geophys. Res. Space Physics*, *118*, 2593-2617, doi:10.1002/jgra.50249.
38. Yiğit, E., and A.S. Medvedev (2010), Internal gravity waves in the thermosphere during low and high solar activity: Simulation study, *J. Geophys. Res.*, *115*, A00G02, doi:10.1029/2009JA015106.
39. Yiğit, E., and A.S. Medvedev (2015), Internal wave coupling processes in Earth's atmosphere, *Advances in Space Research*, *55(4)*, 983-1003, ISSN 0273-1177, <http://dx.doi.org/10.1016/j.asr.2014.11.020>.
40. Yue, J., and W. Wang (2014), Changes of thermospheric composition and ionospheric density caused by quasi-2-day wave dissipation, *J. Geophys. Res. Space Physics*, *119*, 20692078, doi:10.1002/2013JA019725.

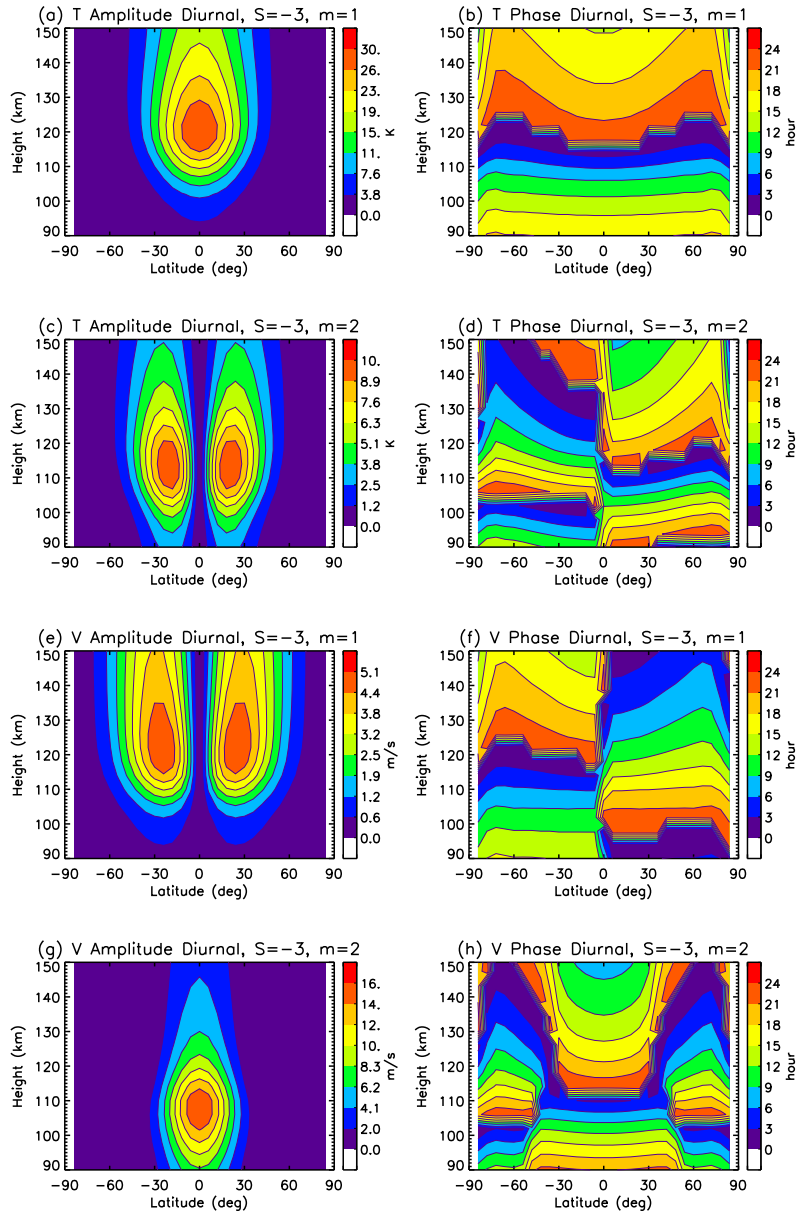


**Fig. 1** DE3 HME amplitudes (left) and phases (right) for temperature (T) and meridional wind (V). (a), (b): First symmetric T. (c), (d): First antisymmetric T. (e), (f): First symmetric V. (g), (h) First antisymmetric V.

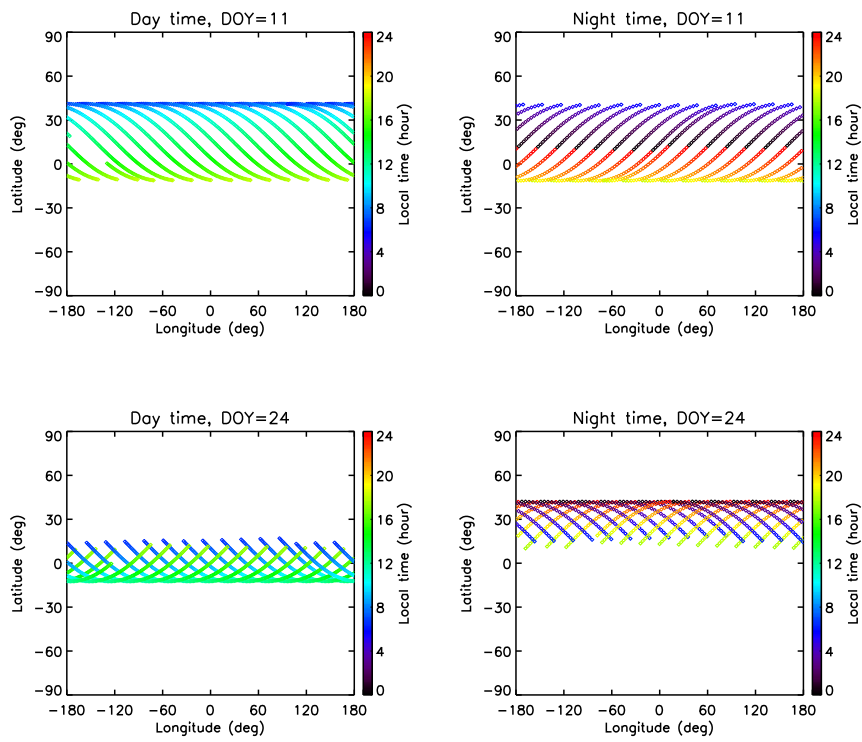


**Fig. 2** Samples of ICON daytime (left) and nighttime (right) sampling of 2009 MERRA-forced TIMEGCM simulation for day of year (DOY) 11 (top) and 24 (bottom).

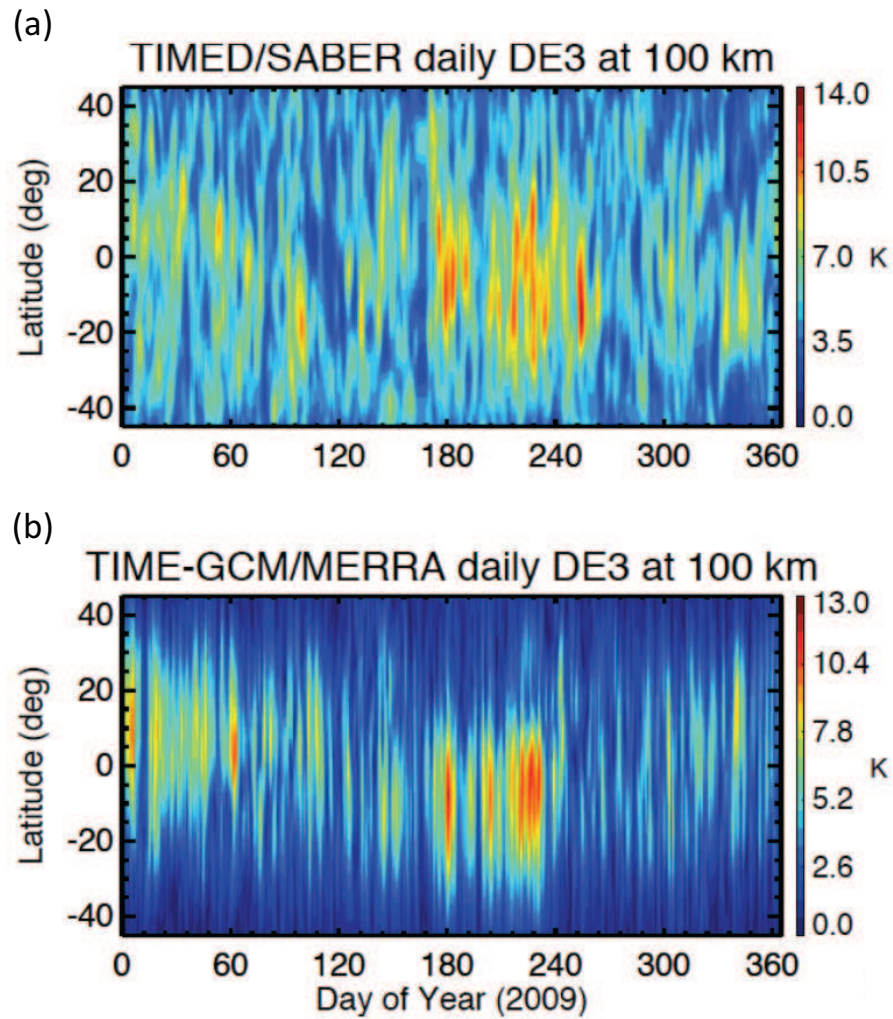


**Fig. 3** Comparison of approximate daily DE3 temperature amplitudes at 100 km from TIMED/SABER (top) and MERRA-forced TIMEGCM (Bottom). The daily TIMED/SABER DE3 amplitudes are estimated by taking temperature differences between observations along ascending and descending parts of the TIMED orbit. See text for further details.

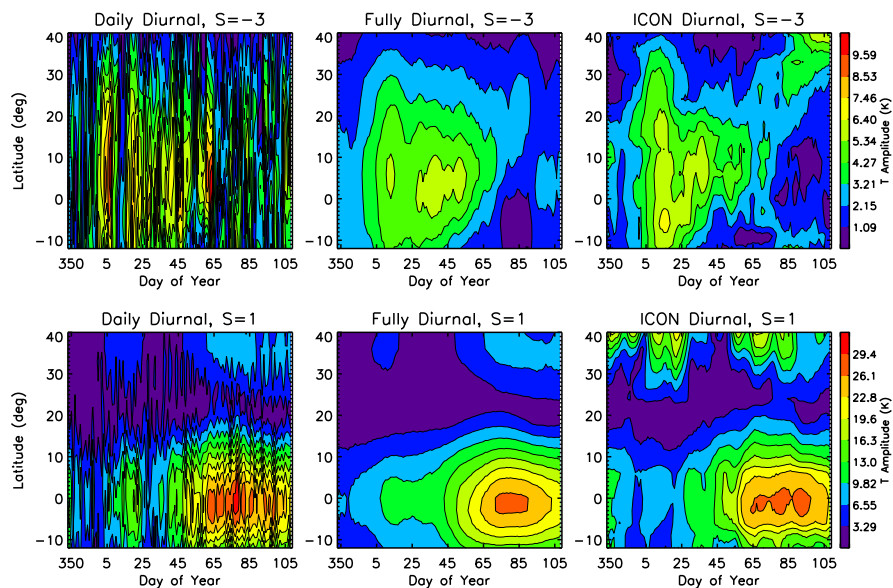


**Fig. 4** DE3 (top) and DW1 (bottom) tidal temperatures at 98 km from 2009 MERRA-forced TIMEGCM simulation for DOY 350-105 Left: daily amplitudes. Middle: 27-day running mean amplitudes obtained from full sampling of the model. Right: Same as middle panel, except for ICON sampling of the model.

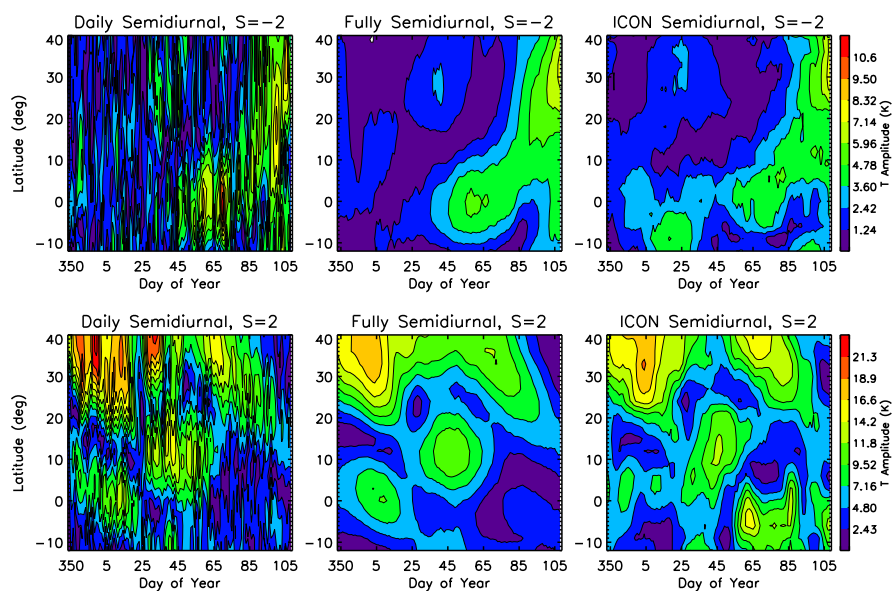


**Fig. 5** Same as Figure 4, except for SE2 (top) and SW2 (bottom).

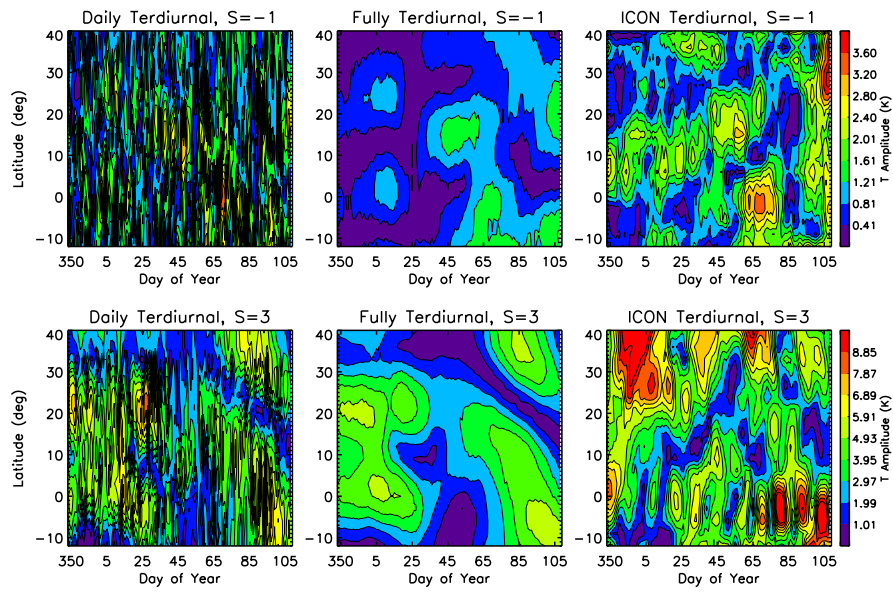
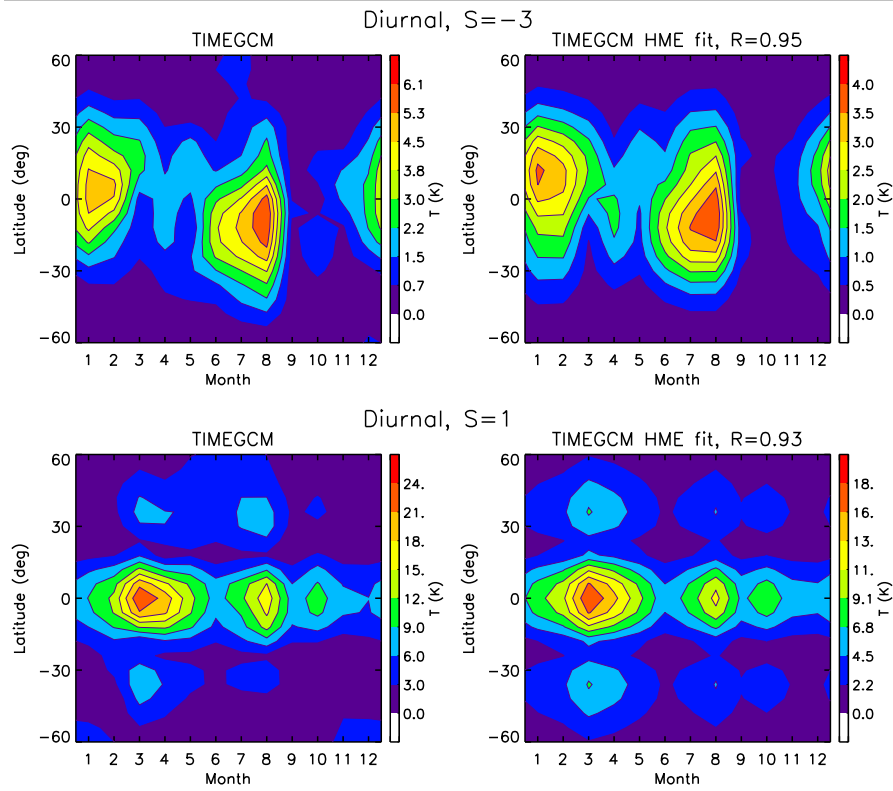
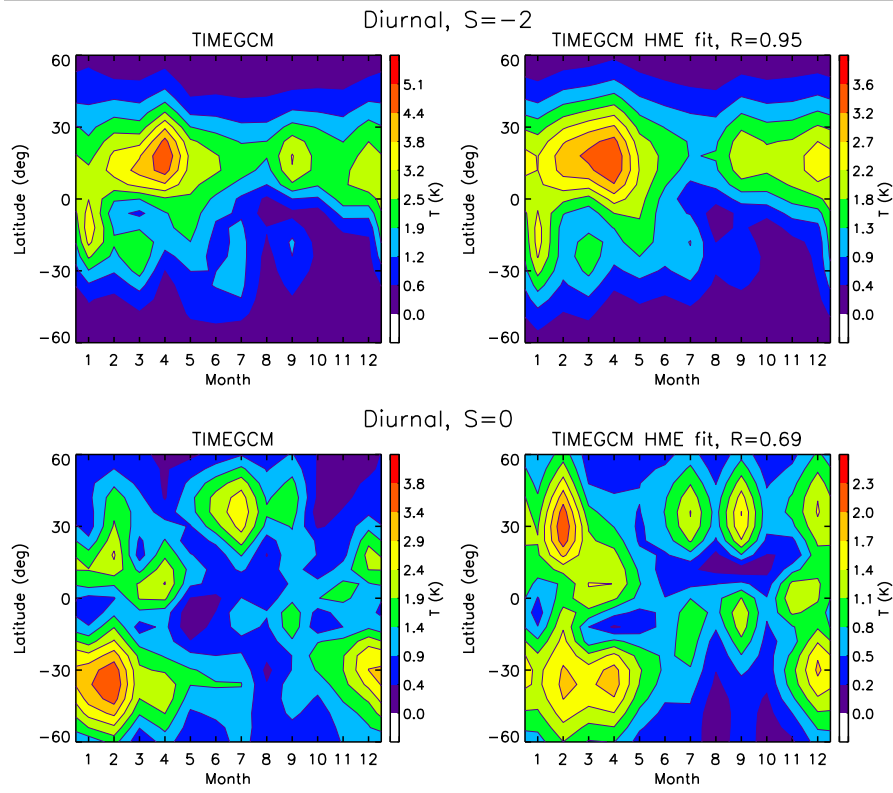


Fig. 6 Same as Figure 4, except for TE1 (top) and TW3 (bottom).



**Fig. 7** Top left: DE3 temperature amplitudes at 98 km from 2009 MERRA-forced TIMEGCM. Top right: Same as top left, except reconstructed from HMEs obtained by fitting model DE3 tidal temperature structures between 12°S and 42°N. Bottom: same as top two panels, except for DW1. The coefficient of correlation (R) between the left and right panels is also indicated.



**Fig. 8** Same as Figure 7, except for DE2 (top) and D0 (bottom).

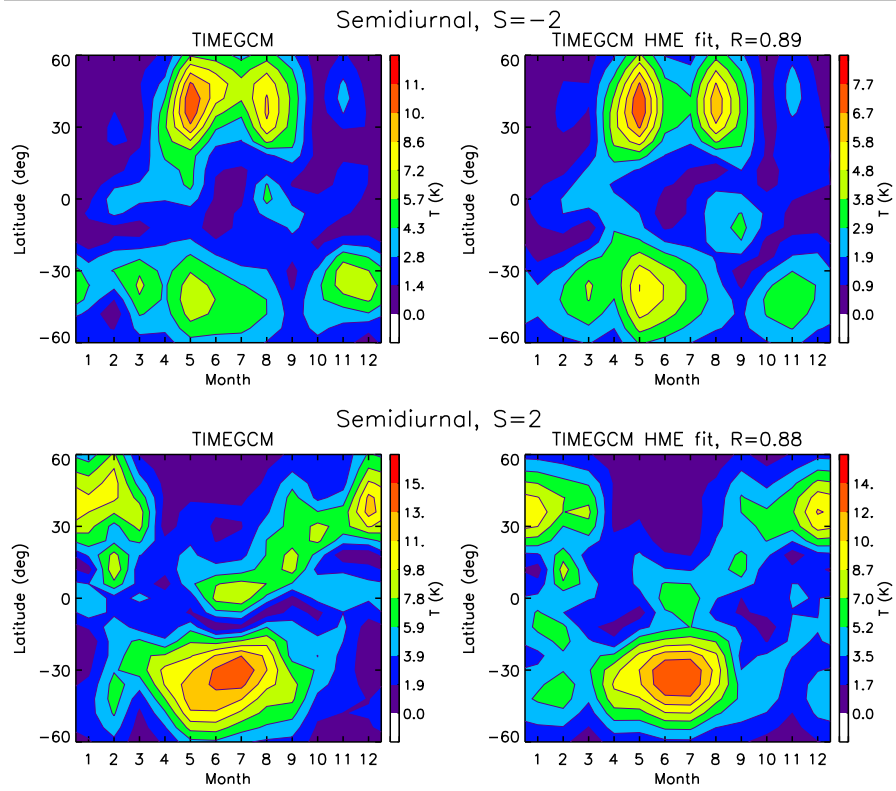


**Fig. 9** Same as Figure 7, except for SE2 (top) and SW2 (bottom).

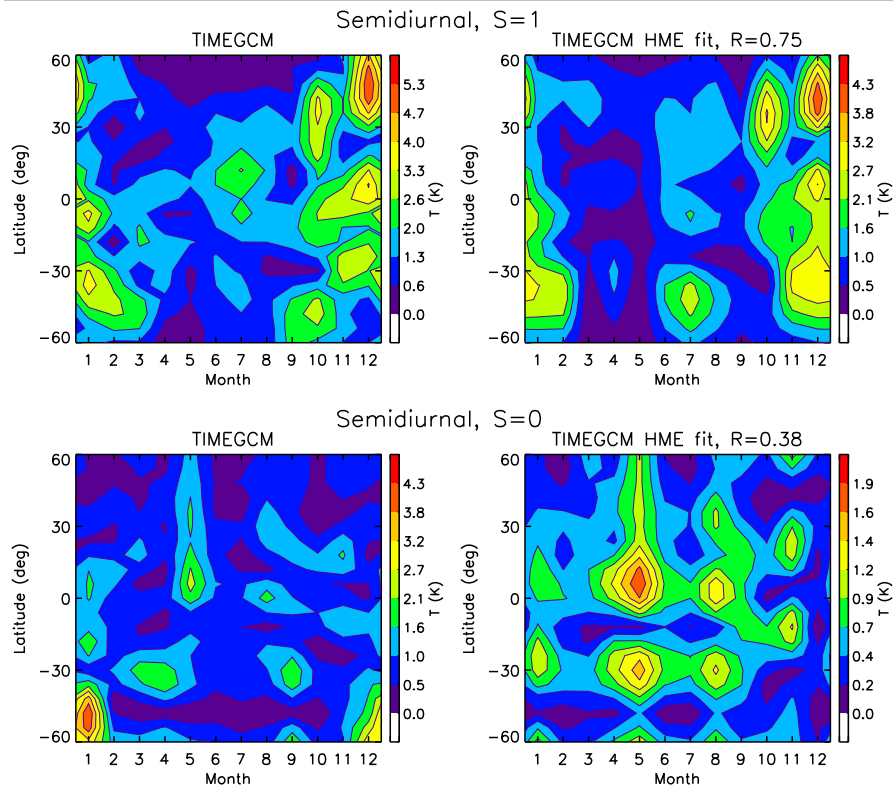


**Fig. 10** Same as Figure 7, except for SW1 (top) and S0 (bottom).

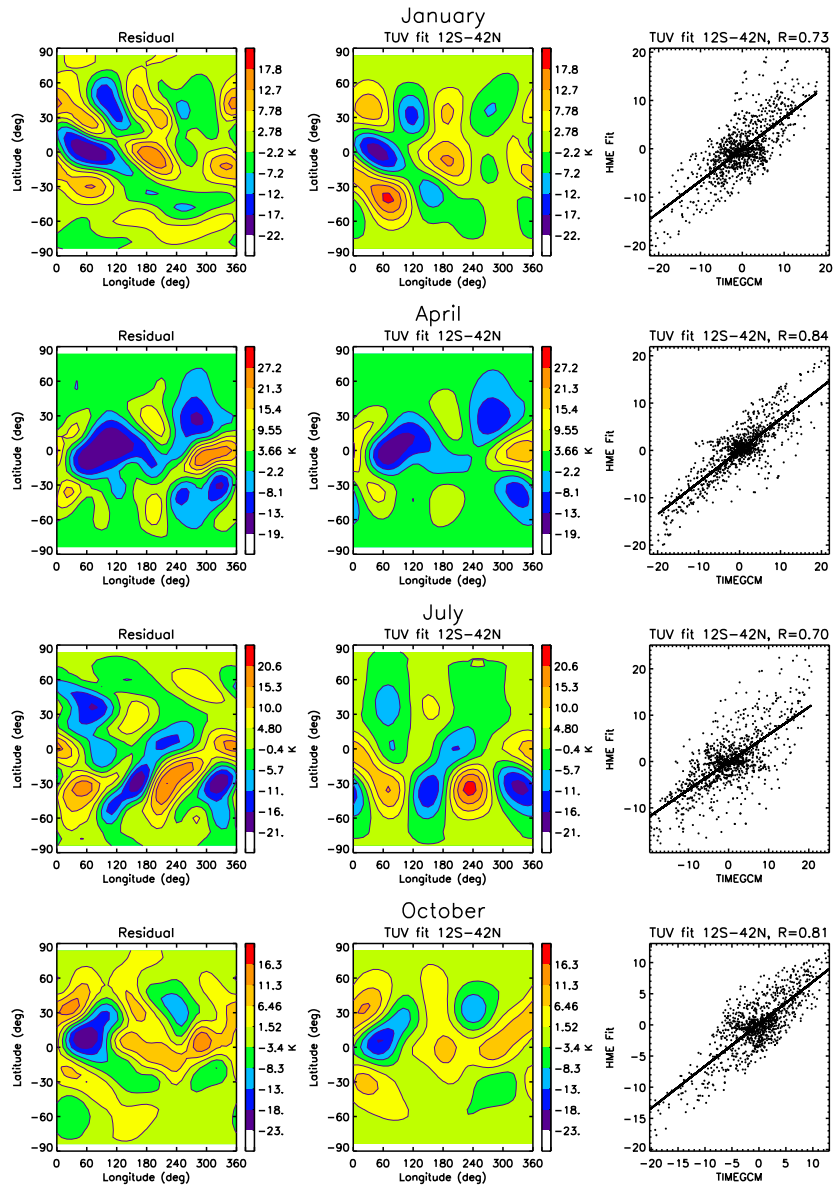


**Fig. 11** Latitude vs. longitude depictions of temperature residuals from longitudinal averages based on 27-day means centered on the 15th day of (top to bottom) January, April, July and October at 0000 UT. Left panels depict TIMEGCM outputs, whereas middle panels depict residuals reconstructed from HMEs obtained by fitting model DE3 tidal temperature structures between  $12^{\circ}\text{S}$  and  $42^{\circ}\text{N}$ . Right panels include scatter diagrams and correlation coefficients based on the two panels to the left.